Influence of manganese (Mn) substitution on structural, infrared and dielectric properties of $BaTiO_3$ nanoceramics

Published: 27 September 2020

Volume 31, pages 19756–19763, (2020) Cite this article

Journal of Materials Science: Materials in Electronics

Aims and scope

Submit manuscript

Smita P. More, Mangesh V. Khedkar, Deepali D. Andhare, Ashok V. Humbe & K. M. Jadhav

Abstract

In the present study, pure barium titanate (BT) and Mn-doped barium titanate nanoceramics were synthesized by sol–gel auto-combustion method. X-ray diffraction (XRD) technique was employed to identify the phase purity and crystal structure of prepared nanoparticles. The analysis of XRD suggests that the sample $x = 0.00, 0.05$ possess a tetragonal structure with

space group *P4mmm*, while $x = 0.15, 0.25$ shows the hexagonal structure with space group *P63mmc*. Using XRD data, the lattice constant '*a*' and '*c*' was determined for all the samples. The other structural parameters such as *c*/*a* unit cell volume, crystallite size, X-ray density, and lattice strain, were also obtained using XRD data. The dielectric study was carried out using LCR-Q meter as a function of frequency. All the dielectric parameters get decreased with increasing frequency. Thus, the doping of Mn in $BaTiO_3$ leads to phase transformation from tetragonal to hexagonal structure and shows strong frequency dependence.

1 Introduction

Amongst the ferroelectric materials, $BaTiO_3$ (BT) perovskite structures are of current interest to the scientist and technologists as they exhibit excellent ferroelectric, dielectric properties piezoelectric, and electro-optic [1]. These materials are widely studied by many researchers. They have been used by various electronic devices such as ceramics, capacitors, sensors, and transducers, pyroelectric detectors, memory cells, capacitors, dielectric resonators,

electromechanical systems, fillers, etc. [2,3,4].

$BaTiO_3$ belongs to ABO_3 type perovskite ferroelectric materials where A and B represent cations of different sizes and values (where A is Ba and B is Ti) where structure possesses 6-fold co-ordinates is cation in the middle, 12-fold co-ordinates A cation in the center and anion oxygen in the center of the face [5]. The packing of the ions can be thought of as the A and O lie together forming close-packed structure. $BaTiO_3$ exhibits different structures at different temperatures. In between 0 °C and 130 °C it exhibits tetragonal structure. It shows cubic structure above 130 °C. It exhibits rhombohedral structure, when temperature is greater than − 90 °C, above 1460 °C it exhibits hexagonal structure [6].

The difference is radii of A and B can lead to various types of structure and also the properties can be altered by doping a suitable cation at A and B site. The method of preparation also influences the ferroelectric properties of $BaTiO_3$. Usually, $BaTiO_3$ precisely studied by many researchers. In recent years, wet chemical methods such as sol–gel auto-combustion, chemical methods have been used to produce nanopowder of $BaTiO_3$ [7]. The advantages of this technique are that it produces powder of nano-scale dimension, more homogeneous, highly lour, and better control over stoichiometry [8]. The properties of $BaTiO_3$ can greatly be affected by its microstructure and in turns synthesis method. The calcinations time and temperature are also one of the key parameters in controlling the properties of $BaTiO_3$.

$BaTiO_3$ has been widely studied by many researchers because of their potential applications in various fields. Many attempts were made to improve the room temperature ferroelectric properties of $BaTiO_3$ by doping of different cations. Many doping elements can be incorporated into the structure of $BaTiO_3$ to improve tailor-made properties [9].

In literature, Sr, Pb, Ca elements have been doped at A site in the view to obtain enhanced ferroelectric properties. Recently transition metal such as Fe, Co, Ni, Mn, etc. has attracted the attention of scientists as they lead to the ferromagnetic appearance along with ferroelectric. Such materials are useful in electronic device applications. Mn-doped $BaTiO_3$ ferroelectric materials have been investigated recently in many researchers [10,11,12]. Alexander Semenov et al. [13] studied the thermal and electoral properties of Mn-doped $BaTiO_3$ ceramics for the multicaloric applications. Son et al. [14] prepared Mn-doped $BaTiO_3$ nanorods which are useful

in four state multiferroic memories. Nageri et al. [15], synthesized manganese doped barium titanate nanotube and reported the enhanced Photocatalytic activity. In our group, we have investigated the effect of Fe doping on various properties of $BaTiO_3$. The results show the simultaneous existence of tetragonal and hexagonal structure for Fe doping [8].

No systematic investigations of crystal structure, infra-red, and dielectric properties of Mn-doped $BaTiO_3$ are reported in the literature. In the present study, we report the low-temperature synthesis of the Mn-doped $BaTiO_3$ using sol–gel auto-combustion method and the results of the investigation of structural, infra-red, and dielectric properties are reported in this work.

2 Experimental

2.1 Materials

Analytical grade barium nitrate hexahydrate ($Ba(NO_3)_2{\cdot}6H_2O$, 99%), tetra butyl titanate ($Ti(OC_4H_9)_4$, 99.9%, Alfa Aesar), Manganese(II) nitrate tetrahydrate ($Mn(NO_3)_3{\cdot}4H_2O$), citric acid ($C_6H_8O_7$, 99.57%) ethanol (C_2H_5–OH, 99%) and ammonium hydroxide (NH_4OH, 99%) were used without further purification.

2.2 Preparation of $BaTi_{1-x}Mn_xO_3$ nanoceramics

$BaTi_{1-x}Mn_xO_3$ nanoceramics with composition (x = 0.00, 0.05, 0.15, and 0.25) were synthesized by safe and easier sol–gel auto combustion technique. Firstly, tetra butyl titanate solution diluted with ethanol was added into the aqueous solution of citric acid. After being stirred at 80 °C for 1 h, a yellowish transparent liquid was obtained which is marked as solution (A). At the same time, barium nitrate and manganese nitrate were dissolved into deionized water and mixed to form an aqueous solution, which is marked as solution (B). Subsequently, solutions A and B were poured together. At the same time, the pH value was adjusted to be 7 (pH = 7) using ammonia until a transparent liquid was achieved. The synthesis protocol was followed by continuous stirring for 3 hr on the magnetic hot plate, stirrer to increase the viscosity of solution gradually, and then a stable transparent sol was formed. Continuous heating of ~ 110 °C initiates the gel formation. Under the constant stirring and heating, the viscous gel transforms into a dry gel. The gel formed from metal nitrates and

citric acid exhibited self-propagating combustion behavior, and the entire combustion process was done in a few seconds. The obtained powders were dried, crushed, and were sintered at 1100 °C for 6 h in a muffle furnace to get the nanocrystalline powders. Figure 1 presents the flow chart of the sol–gel synthesis of $BaTi_{1-x}Mn_xO_3$ nanoceramics.

Fig. 1

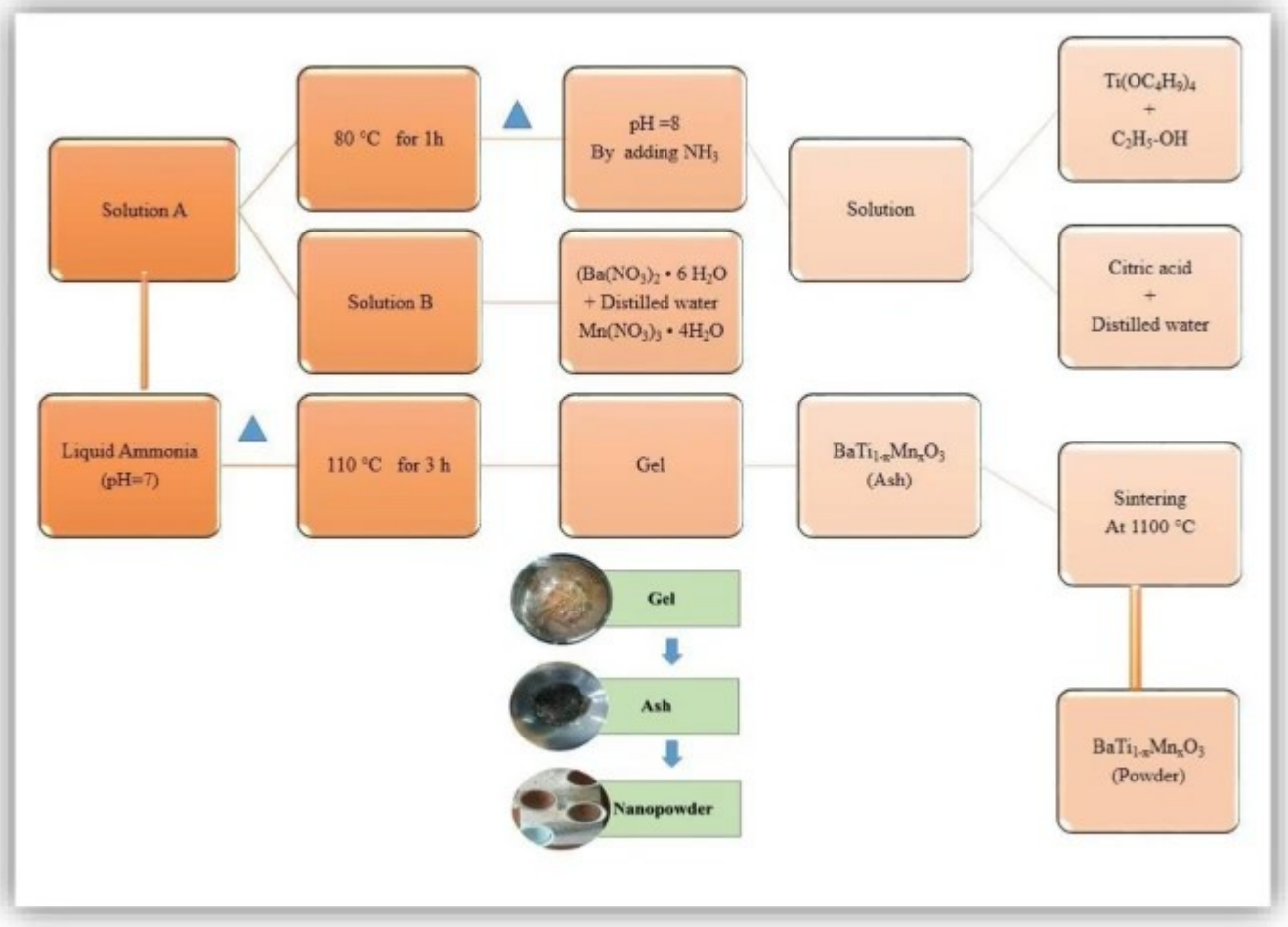

Flowchart of synthesis of $BaTi_{1-x}Mn_xO_3$ ($x = 0.00–0.25$) nanoceramics

2.3 Characterization

The prepared $BaTi_{1-x}Mn_xO_3$ ($x = 0.00$, 0.05, 0.15, and 0.25) nanoparticles was characterized by using XRD, FT-IR, and dielectric properties. Crystalline phases of the samples were examined by X-ray diffraction (XRD) pattern obtained using the Rigaku X-ray diffractometer at room

temperature. The pattern was recorded using Cu-K_α radiation (λ = 1.54182 Å) in the 2θ range 20°−80° with step size 0.01° and time/step 2 s. Fourier transform infrared spectroscopy (FTIR) of the prepared samples were recorded in the wavenumber range 4000−400 cm^{-1} on Bruker spectrophotometer using KBr as reference material. The dielectric properties of all the samples were measured using the LCR-Q meter (Hioki 3532-50, Japan) as a function of frequencies in the range 50 Hz−5 MHz at room temperature.

3 Results and discussion

3.1 X-ray diffraction (XRD)

Figure 2 show X-ray diffraction (XRD) patterns of powder of all Mn-doped $BaTiO_3$ samples. A close examination of XRD patterns reveals the formation of a single-phase compound. No extra peak has been identified in the XRD patterns. All the diffraction peaks of pure $BaTiO_3$ and Mn-doped $BaTiO_3$ are well indexed. The sample with x = 0.00 and 0.05 shows the tetragonal structure with the *P4mmm* space group. The XRD patterns well match with JCPDS 79-2264. The sample with x = 0.15 and 0.25 is indexed to hexagonal structure with space group P63mmc and matches with JCPDS 82-1175. Further, it is also observed from the XRD pattern that the peak (110) is shifted to the left side (lower angle). The shifting of the peak is shown in Fig. 2b. This peak indicates the successful incorporation of Mn at the $BaTiO_3$. For x = 0.15 and 0.25, the XRD patterns suggest the existence of a hexagonal structure. Thus, the transformation of phase from tetragonal to hexagonal structure has occurred for a higher concentration of Mn i.e. beyond x = 0.15. In literature, it is reported that for the higher concentration of Mn both tetragonal and hexagonal phases are present [16].

The lattice parameters ‘a’ and ‘c’ for x = 0.00 and 0.05 were calculated using the following formula for tetragonal structure [7],

$$\frac{1}{{d}^{2}}= \frac{{h}^{2}+ {k}^{2}}{{a}^{2}}+ \frac{{l}^{2}}{{c}^{2}},$$

(1)

where d is interplanar spacing ‘a’ and ‘c’ lattice constant, ($h\,k\,l$) are Miller indices.

The values of lattice parameters ('*a*' and '*c*'), *c/a* ratio, unit cell volume (*V*) and X-ray density (ρ_X) are listed in Table 1. It is evident from Table 1 that both '*a*' and 'c' increased for tetragonal structure and decreased for hexagonal structure. This variation in lattice constant is attributed to the oxidations states of Mn ions incorporated in $BaTiO_3$. It is very well known that the ionic radius Ti^{4+} is 0.605 Å. The incorporation of Mn ions in $BaTiO_3$ may lead to the presence of Mn^{2+}, Mn^{3+} and Mn^{4+} with effective ionic radii as 0.80 Å, 0.66 Å and 0.60 Å, respectively [17]. In general, incorporation of Mn^{2+} and Mn^{3+} with greater ionic radii replaces Ti^{4+} which enhances the lattice parameters, whereas the incorporation of Mn^{4+} with a smaller ionic radius decreases the lattice parameters. Thus, in present case it is revealed that all these three oxidation states of Mn are present in our samples and the variation in Mn concentration in $BaTiO_3$ lattices is responsible to the change of the lattice parameters. Similar behavior of lattice parameters is reported in the literature [18]. Further, c/a ratio was also calculated and its values are listed in Table 1. The ratio c/a is more than one which indicates the tetragonal structure of $BaTiO_3$. For $x = 0.00$, 0.05 samples. Variation of lattice constant '*a*' and '*c*' concerning the Mn concentration is shown in Fig. 3. For $x = 0.15$ and 0.25 the lattice constant was determined by the following relation [19] and their values are given in Table 1. It is observed that lattice constant decreases as composition *x* increases.

Table 1 Values of lattice parameters ('a' and '*c*'), *c/a* ratio, unit cell volume (*V*) and X-ray density (ρ_X) of $BaTi_{1-x}Mn_xO_3$ nanoceramics

$$\frac{1}{{d}^{2}}= \frac{4}{3}\left(\frac{{h}^{2} + hk + {k}^{2}}{{a}^{2}}\right)+ \frac{{l}^{2}}{{c}^{2}}$$

(2)

The other structural parameters like X-ray density, unit cell volume, and lattice strain were also calculated using XRD data. The unit cell volume (*V*) was calculated using the following relation [11],

$$V={a}^{2}\text{c}$$

(3)

The values of unit cell volume are given in Table 1. Like lattice constant unit, unit cell volume also decreases as x increases from $x = 0.00$ to 0.05 as well as $x = 0.15$ to 0.25.The X-ray density (ρ_X) was determined by the following relation [20] and obtained values are listed in Table 1.

$${\rho }_{x}=\frac{ZM}{{N}_{\rm A}V},$$

(4)

where Z is the number of formula units in the unit cell, M is the molecular mass of the sample and N_A is the Avogadro's number. It can be observed from Table 1 that the X-ray density decreases with an increase in x. The lattice strain (ε) was also calculated using relation [21],

$$\varepsilon =\frac{\beta \cos\theta }{4}$$

(5)

where ε is the root mean square value of lattice strain, β is the full width of peak half maxima and θ is peak position. The calculated values are presented in Table 2. The crystallite size (t) was determined using the Debye–Scherrer's formula [22],

Table 2 Values of 2θ (degree), FWHM, the average crystallite size (t), lattice strain (ε) of $BaTi_{1-x}Mn_xO_3$ nanoceramics

$$t=\frac{0.9 }{\beta \cos\theta },$$

(6)

where λ is the wavelength of Cu-K_α radiation, β is the full width of the half maximum and θ is the Braggs angle. The crystallite size was found to be in the range of 5–8 nm. The calculated values of crystallite size are presented in Table 2.

Fig. 2

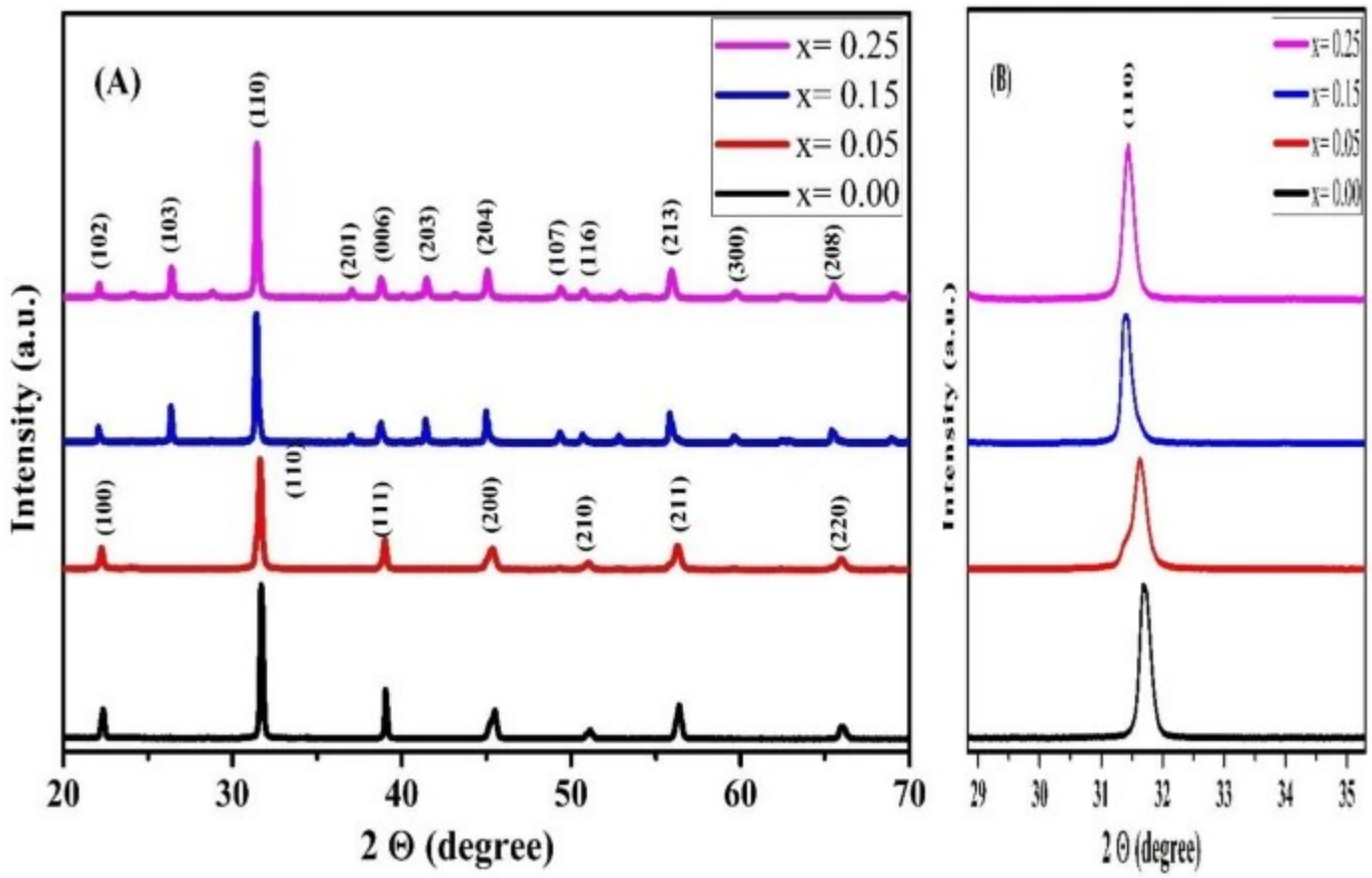

a XRD patterns for Mn-doped $BaTi_{1-x}Mn_xO_3$ and b shifting of (110) peak

Fig. 3

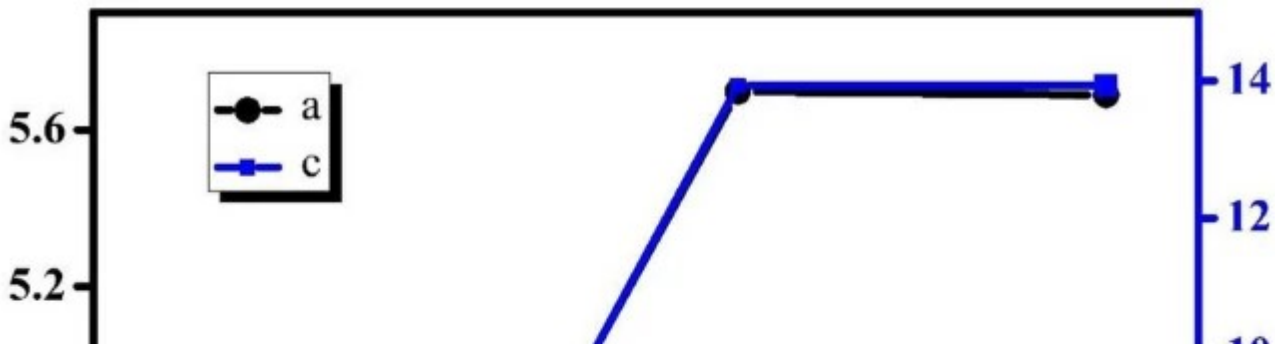

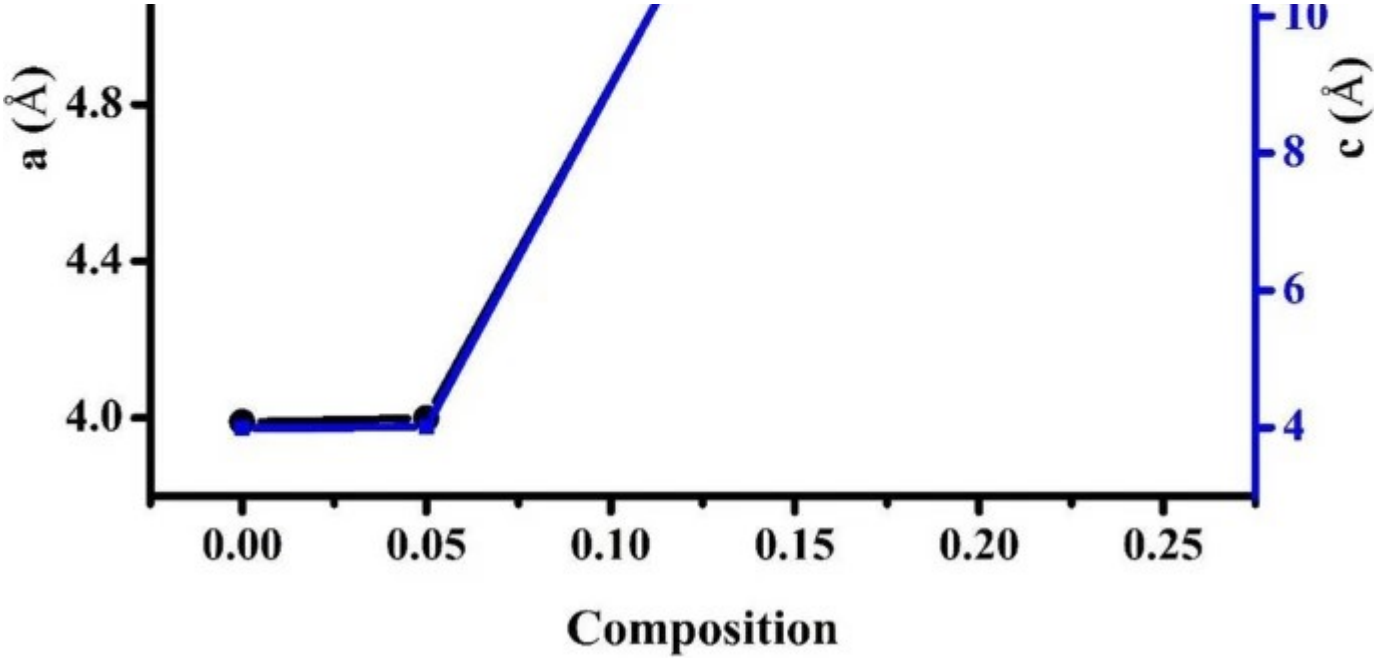

Variation of lattice constant *a* and *c* with Mn composition *x*

3.2 FT-IR studies

Figure 4 represents Fourier transform Infrared spectroscopy (FT-IR) of all the samples under investigation recorded in the range 400–4000 cm^{-1} at room temperature. The spectra shows four prominent bands near 600 cm^{-1}, 1500 cm^{-1}, 2335 cm^{-1} and 3700 cm^{-1}. The first absorption band (v_1) near 600 cm^{-1} corresponds to Ti–O stretching vibrations in all the samples. The second absorption (v_2) band near to 1500 cm^{-1} and this absorption band corresponds to the deformation mode of absorbed water (H_2O) molecules, assigned to the bending vibrations. The third absorption (v_3) band around 2335 cm^{-1} corresponds to C–O stretching vibrations. The fourth absorption (v_4) band around 3700 cm^{-1} has been assigned to O–H stretching (symmetric and asymmetric) vibrations hydrogen-bonded OH groups. Table 3 represents the peak position corresponds to absorption bands. Further, it is also noticed from FTIR spectra that with doping Mn in $BaTiO_3$ only shifting in absorption band is observed. Our results are enclosed agreement with that of the reported literature [13].

Table 3 Absorption bands values for $BaTi_{1-x}Mn_xO_3$ nanoceramics

Fig. 4

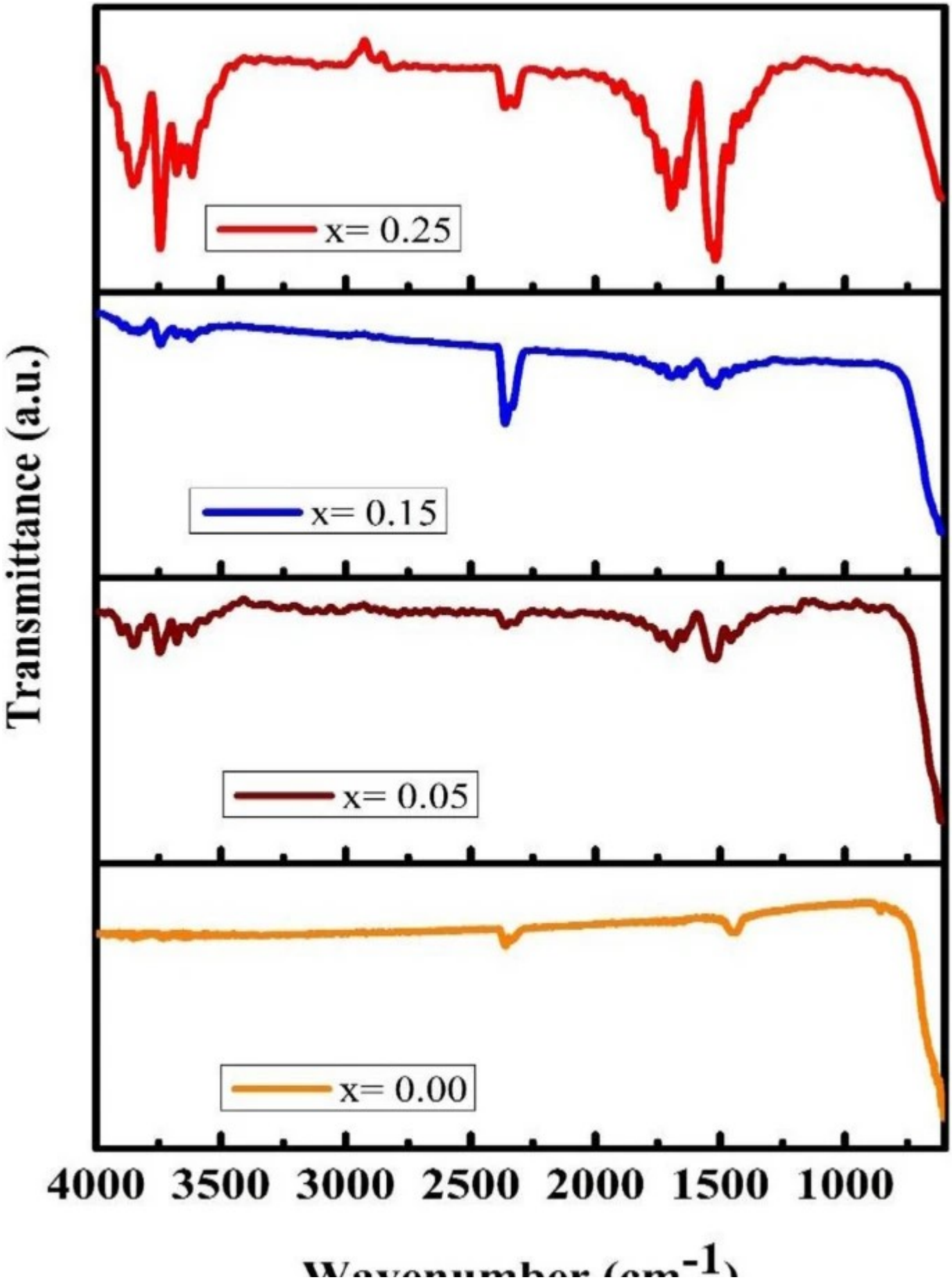
x= 0.25
x= 0.15
x= 0.05
x= 0.00
Transmittance (a.u.)
4000 3500 3000 2500 2000 1500 1000
Wavenumber (cm-1)

FT-IR spectra of $BaTi_{1-x}Mn_xO_3$

3.3 Dielectric studies

$BaTiO_3$ are the good ferroelectric materials having the dielectric properties of Mn-doped $BaTiO_3$ were studied at room temperature using LCR-Q meter in the frequency range 50 Hz to 5 MHz. The real part of dielectric constant ε' was calculated using the following relation [23],

$${\varepsilon }^{\prime}=\frac{C_{\rm t}}{{\varepsilon }_{0}A},$$

(7)

where C is the capacitance of pellet, t is the thickness of the specimen, A is the area of cross-section of the pallet and ε_0 is the permittivity of free space. Figure 5 represents the variation of dielectric constants as a function of frequency and the inset shows a partially enlarged image of the low frequency to intermediate-range frequency. The pure sample ($BaTiO_3$) possesses a high dielectric constant that is 653 at 50 Hz frequency. Figure 5 shows that at low frequencies all samples show high dielectric constant it may be due to voids and defects presents in the crystal. It is also observed from the figure with substitution of Mn dielectric constants gets decreases because of Mn^{3+} ions replace Ti^{4+} ions which create oxygen vacancies. That occurred oxygen vacancies leads to break Ti—O bonds causes a reduction in dielectric properties. It is observed from Fig. 5 that dielectric constant decreases with an increase in frequency. The decrease in ε' is exponential and it is in good agreement with the reported literature [11]. Figures 6 and 7 represent the variation of dielectric loss ε'' and dielectric loss tangent ($\tan \delta$). Similar to dielectric constant, the dielectric loss and dielectric loss tangent values also decreases with increasing frequency. It is observed from Fig. 6 that the value of dielectric loss was large at low frequencies. This high dielectric loss below the Curie temperature was mainly caused by domain movement as reported in the previous report [24]. It is well known fact that incorporation of Mn in place of Ti site generates the oxygen vacancies as well as the defects dipolar which stabilizes the domains. The initial decrease in dielectric loss with frequency for all the compositions can be elucidated on the basis of

Maxwell–Wagner interfacial polarization. It was observed previously that the crystallite size and the density of a material was also vital aspects to affect the dielectric characteristics [25, 26]. In addition, besides the effect of the crystallite size, the polarization was also a key factor contributing to the dielectric characteristics [27]. The compositional dependence of ε', ε'' and tan δ is shown in Table 4. It is clear from the table that all these dielectric parameters decrease in Mn doping concentration increases.

Table 4 The compositional dependence of dielectric constant (ε'), dielectric loss (ε'') and dielectric loss tangent (tan δ) for $BaTi_{1-x}Mn_xO_3$ nanoceramics

Fig. 5

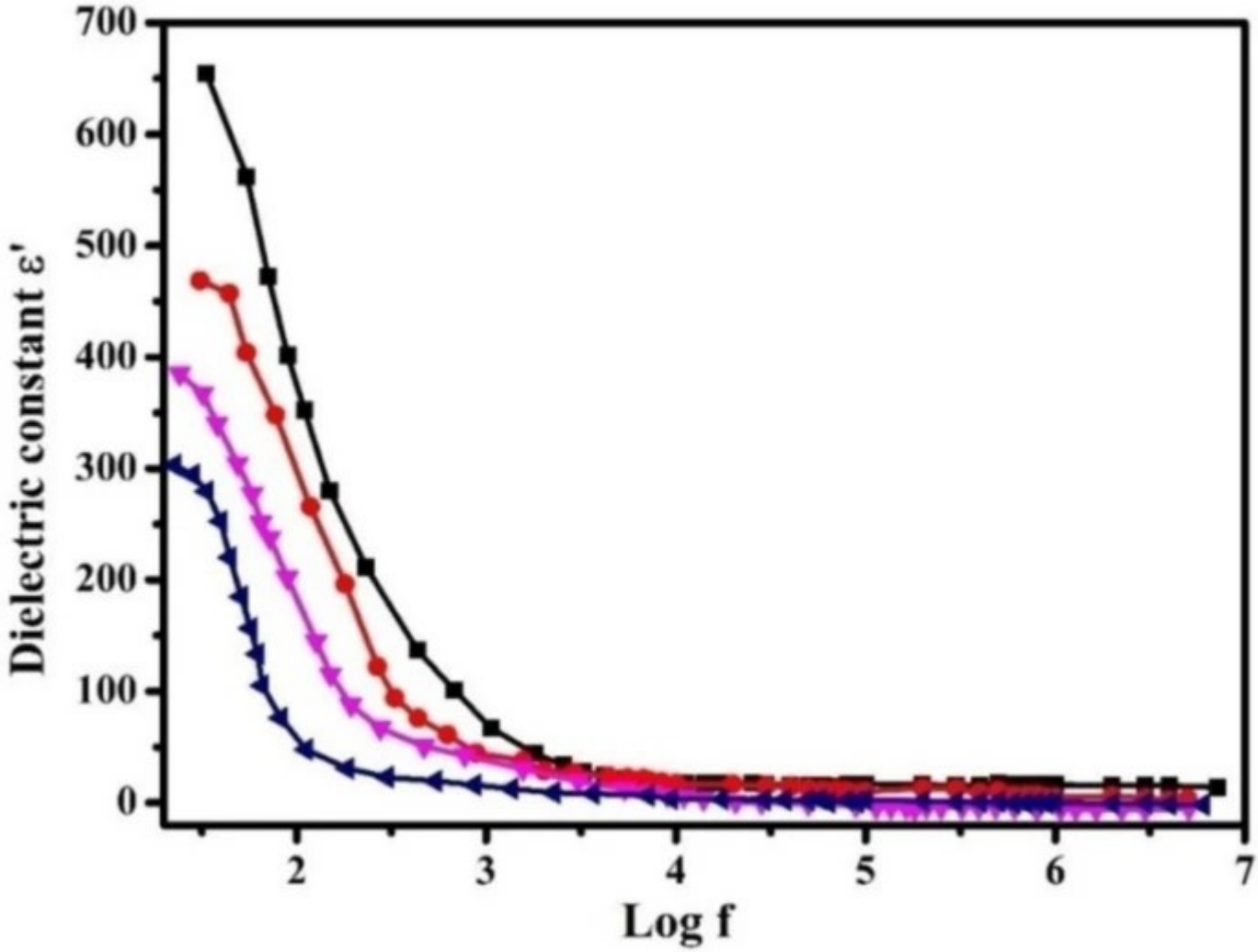

Variation of dielectric constant (ε') with frequency at room temperature of $BaTi_{1-x}Mn_xO_3$ ($x = 0.00-0.25$) nanoceramics (The inset shows partially enlarged image)

Fig. 6

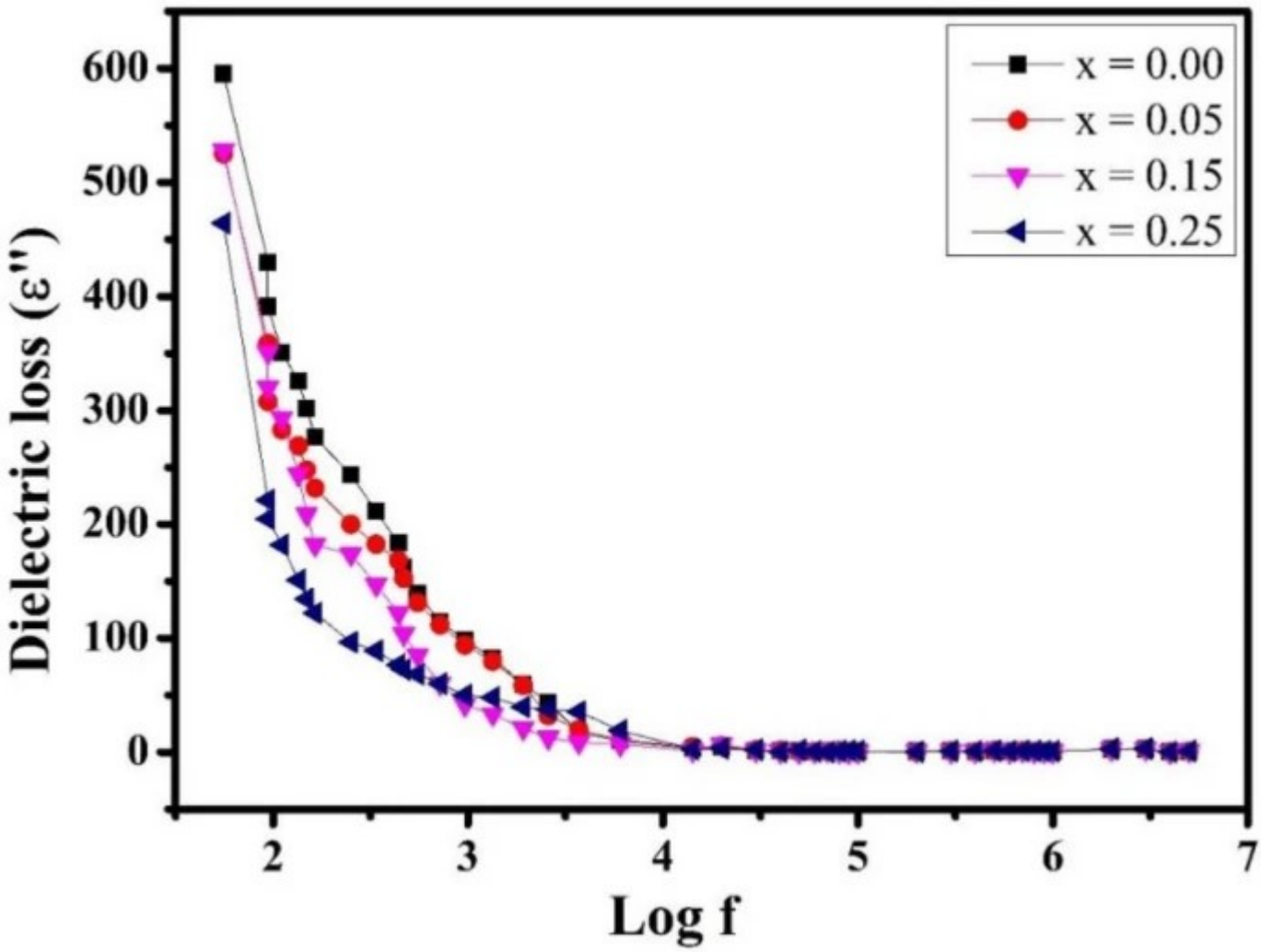

Variation of dielectric loss (ε'') with frequency at room temperature of $BaTi_{1-x}Mn_xO_3$ ($x = 0.0-0.5$) nanoceramics

Fig. 7

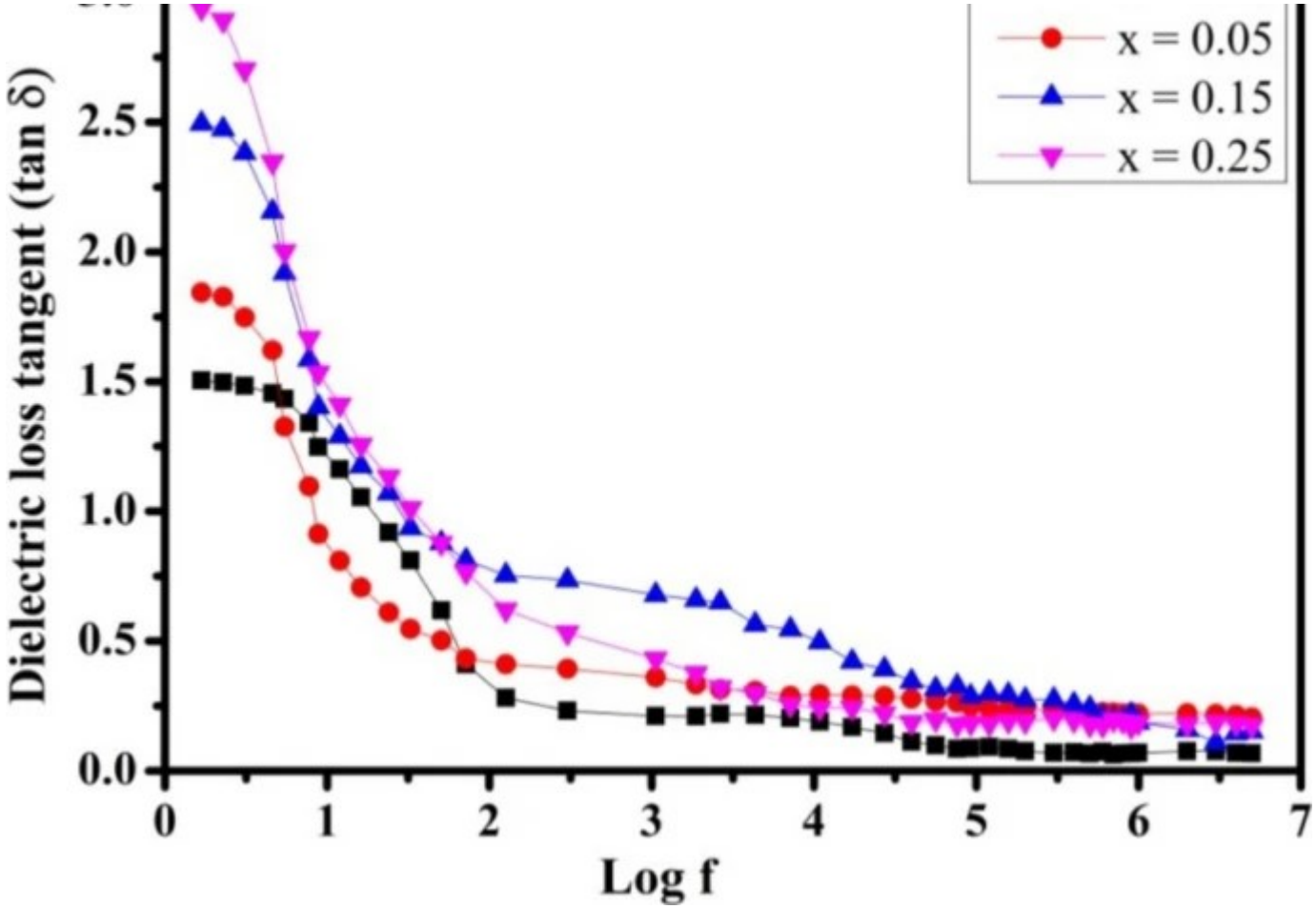

Variation of dielectric loss tangent (tan δ) with frequency at room temperature of $BaTi_{1-x}Mn_xO_3$ (x = 0.0–0.5) nanoceramics

4 Conclusion

The samples of pure $BaTiO_3$ and Mn-doped $BaTiO_3$ in nanocrystalline form were successfully synthesized using the sol–gel auto-combustion method. The resultant nanopowder has high chemical homogeneity, better crystallinity, and lower average crystallite size. All the samples were successfully characterized by an X-ray diffraction technique exhibiting single-phase nature with the tetragonal structure for x = 0.00, 0.05, and hexagonal structure for x = 0.15 and 0.25. Thus, the phase transformation from tetragonal to hexagonal occurs from x = 0.05 onwards. The FT-IR spectra reveal the characteristic feature of ferroelectric Barium titanate showing four absorption bands at around 600 cm^{-1}, 1500 cm^{-1}, 2335 cm^{-1} and 3700 cm^{-1}. The dielectric constant, dielectric loss and dielectric loss tangent get decreases with increasing

frequency.

References

1. H. Qi et al., Superior energy-storage capacitors with simultaneously giant energy density and efficiency using nanodomain engineered $BiFeO_3$-$BaTiO_3$-$NaNbO_3$ lead-free bulk ferroelectrics. Adv. Energy Mater. 10(6), 1903338 (2020)

Article CAS Google Scholar

2. G.H. Haertling, Ferroelectric ceramics: history and technology. J. Am. Ceram. Soc. 82(4), 797–818 (1999)

Article CAS Google Scholar

3. R. Whatmore et al., Ferroelectric thin films for capacitor and sensor applications. NATO ASI Ser. E Appl. Sci. Adv. Study Inst. 284, 383–398 (1995)

CAS Google Scholar

4. T.Q. Trung, N.E. Lee, Flexible and stretchable physical sensor integrated platforms for wearable human-activity monitoring and personal healthcare. Adv. Mater. 28(22), 4338–4372 (2016)

Article CAS Google Scholar

5. K. Anjali, Solid-state NMR studies at the structural phase transition region of ferroelectric materials. PhD Thesis (2016)

6. R.J. Tilley, *Perovskites: Structure-Property Relationships* (Wiley, Chichester, 2016)

Book Google Scholar

7. D.N. Bhoyar et al., Structural, infrared, magnetic and ferroelectric properties of $Sr_{0.5}Ba_{0.5}Ti_{1-x}Fe_xO_3$ nanoceramics: modifications via trivalent Fe ion doping. Physica B 581, 411944 (2020)

Article CAS Google Scholar

8. P.P. Khirade et al., Multiferroic iron doped $BaTiO_3$ nanoceramics synthesized by sol–gel auto combustion: influence of iron on physical properties. Ceram. Int. 42(10), 12441–12451 (2016)

Article CAS Google Scholar

9. N. Wang et al., Investigation of structural, ferroelectric and magnetic properties of Ca modified $BiFeO_3$–$BaTiO_3$ ceramics. Ceram. Int. 46(3), 3855–3860 (2020)

Article CAS Google Scholar

10. X. Yuan et al., Tuning ferroelectric, dielectric, and magnetic properties of $BiFeO_3$ ceramics by Ca and Pb co-doping. Phys. Status Solidi (B) 256(3), 1800499 (2019)

Article Google Scholar

11. M. Arshad et al., Fabrication, structure, and frequency-dependent electrical and dielectric properties of Sr-doped $BaTiO_3$ ceramics. Ceram. Int. 46(2), 2238–2246 (2020)

Article CAS Google Scholar

12. C. Zhu et al., High energy density, high efficiency and excellent temperature stability of

lead free Mn-doped $BaTiO_3$–$Bi(Mg_{1/2}Zr_{1/2})O_3$ ceramics sintered in a reducing atmosphere. J. Alloys Compd. 816, 152498 (2020)

Article CAS Google Scholar

13. M. Amin, *Exploring the Multifunctional Properties of $BiFeO_3$-Based Multiferroics* (University of the Punjab, Lahore, 2019)

Google Scholar

14. J.Y. Son et al., Four-states multiferroic memory embodied using Mn-doped $BaTiO_3$ nanorods. ACS Nano 7(6), 5522–5529 (2013)

Article CAS Google Scholar

15. M. Nageri, V. Kumar, Manganese-doped $BaTiO_3$ nanotube arrays for enhanced visible light photocatalytic applications. Mater. Chem. Phys. 213, 400–405 (2018)

Article CAS Google Scholar

16. J. Lombardi et al., Stoichiometric control over ferroic behavior in $Ba(Ti_{1-x}Fe_x)O_3$ nanocrystals. Chem. Mater. 31(4), 1318–1335 (2019)

Article CAS Google Scholar

17. R. Shannon, Revised effective ionic radii and systematic studies of interatomic distances in halides and chaleogenides. Acta Crystallogr. A 32(5), 751–767 (1976)

Article Google Scholar

18. T.-L. Phan et al., Influences of annealing temperature on structural characterization and magnetic properties of Mn-doped $BaTiO_3$ ceramics. J. Appl. Phys. 112(1), 013909 (2012)

Article Google Scholar

19. S. Yakout, Influence of Na and Na/Fe doping on the dielectric constant, ferromagnetic and sunlight photocatalytic properties of $BaTiO_{33}$ perovskite. J. Solid State Chem. 290, 121517 (2020)

Article CAS Google Scholar

20. V. Ptashnyk et al., The change of structural parameters of nanoporous activated carbons under the influence of ultrasonic radiation. Appl. Nanosci. (2020). https://doi.org/10.1007/s13204-020-01393-z

Article Google Scholar

21. M. Habib et al., Phase evolution and origin of the high piezoelectric properties in lead-free $BiFeO_3$–$BaTiO_3$ ceramics. Ceram. Int. (2020). https://doi.org/10.1016/j.ceramint.2020.05.301

Article Google Scholar

22. A. Shrivastava et al., Synthesis and structural study of Cr-doped $BaTiO_3$ by X-ray diffraction technique and Williamson–Hall and size strain plot methods, in *AIP Conference Proceedings* (AIP Publishing LLC, College Park, 2019)

23. M. Rizwan et al., Electronic, structural and optical properties of $BaTiO_3$ doped with lanthanum (La): insight from DFT calculation. Optik 211, 164611 (2020)

Article CAS Google Scholar

24. W. Chen et al., Effect of the Mn doping concentration on the dielectric and ferroelectric properties of different-routes-fabricated $BaTiO_3$-based ceramics. J. Alloys Compd. 670,

48–54 (2016)

Article CAS Google Scholar

25. I. Raevski et al., High dielectric permittivity in $AFe_{1/2}B_{1/2}O_3$ nonferroelectric perovskite ceramics (A = Ba, Sr, Ca; B = Nb, Ta, Sb). J. Appl. Phys. 93, 4130–4136 (2003)

Article CAS Google Scholar

26. J. Yang et al., Ultrathin $BaTiO_3$ nanowires with high aspect ratio: a simple one-step hydrothermal synthesis and their strong microwave absorption. ACS Appl. Mater. Interfaces 5, 7146–7151 (2013)

Article CAS Google Scholar

27. Q.-S. Wu et al., A surfactant-free route to synthesize $Ba_xSr_{1-x}TiO_3$ nanoparticles at room temperature, their dielectric and microwave absorption properties. Sci. China Mater. 59, 609–617 (2016)

Article CAS Google Scholar

Acknowledgements

The author Ms. Smita More is very much thankful to the School of Physical Sciences, Solapur University for providing X-ray diffraction and Dr. S.M. Patange, Shrikrishna Mahavidyalaya, Gunjoti, Maharashtra for providing Dielectric properties measurements.

Author information

Authors and Affiliations

Department of Physics, Dr. Babasaheb Ambedkar Marathwada University, Aurangabad, Maharashtra, 431004, India
Smita P. More, Mangesh V. Khedkar, Deepali D. Andhare, Ashok V. Humbe & K. M. Jadhav

Corresponding author

Correspondence to K. M. Jadhav.

Ethics declarations

Conflict of interest

No conflict of interests to declare.

Additional information

Publisher's Note

Rights and permissions

About this article

Cite this article

More, S.P., Khedkar, M.V., Andhare, D.D. *et al.* Influence of manganese (Mn) substitution on structural, infrared and dielectric properties of $BaTiO_3$ nanoceramics. *J Mater Sci: Mater Electron* 31, 19756–19763 (2020). https://doi.org/10.1007/s10854-020-04500-6

Received
24 July 2020

Accepted
14 September 2020

Published
27 September 2020

Issue Date
November 2020

DOI
https://doi.org/10.1007/s10854-020-04500-6